



UKAEA-CCFE-PR(25)376

F. Palermo, F. Casson, F. Koechl, N. Chulu-Chinn, B. McMillan, L. Garzotti, C. Angioni, C. M. Roach

# Electron transport in spherical tokamaks based on stochasticity

Enquiries about copyright and reproduction should in the first instance be addressed to the UKAEA Publications Officer, Culham Science Centre, Building K1/0/83 Abingdon, Oxfordshire, OX14 3DB, UK. The United Kingdom Atomic Energy Authority is the copyright holder.
The contents of this document and all other UKAEA Preprints, Reports and Conference Papers are available to view online free at scientific-publications.ukaea.uk/

## Electron transport in spherical tokamaks based on stochasticity

F. Palermo, F. Casson, F. Koechl, N. Chulu-Chinn, B. McMillan, L. Garzotti, C. Angioni, C. M. Roach

## Electron transport in spherical tokamaks based on stochasticity

F. Palermo <sup>1</sup>, F. Casson<sup>1</sup>, F. Koechl<sup>1</sup>, N. Chulu-Chinn<sup>1,2</sup>, B. McMillan<sup>2</sup>, L. Garzotti<sup>1</sup>, C. Angioni<sup>3</sup>, C. M. Roach<sup>1</sup>

 $^{1}\mathrm{CCFE},$  UKAEA, Culham Science Centre, Abingdon OX14 3EB, UK

 $E\text{-}mail: \\ \textbf{francesco.palermo@ukaea.uk}$ 

November 2024

Abstract. Magnetic stochastic perturbations can strongly influence cross-field transport in high  $\beta$  tokamak plasmas. The impact of stochastic magnetic fields on electron heat transport in MAST/MAST-U is studied over a range in collisionality. Different formulae, based on the Rechester-Rosenbluth and the semi-empirical Rebut-Lallia-Walkins models, are used to describe the stochastic field contribution to electron heat transport, and these expressions are used to supplement TGLF reduced model predictions of the transport from electrostatic turbulence. This more complete anomalous transport model is implemented in the JINTRAC code, and applied to transport simulations of the flat-top phase in MAST/MAST-U. The different ranges of validity of the stochastic transport models are briefly reviewed, focusing on the length-scales involved in the transport process. The principal relevant length-scales have been calculated using the plasma equilibrium characteristics, and used to determine the most appropriate stochastic transport model that is then applied in each shot. This analysis strongly suggests that stochasticity is an important transport mechanism in spherical tokamaks, and that this must be included to model ST plasma scenarios where strong electron heat transport is not described by other instabilities. On the basis of obtained results the importance of stochasticity for the STEP device has been also discussed.

<sup>&</sup>lt;sup>2</sup>University of Warwick, Coventry CV4 7AL, UK

 $<sup>^3{\</sup>rm Max}$  Planck Institut fur Plasmaphysik, Boltzmannstr. 2, 85748 Garching bei Munchen, Germany

## 1. Introduction

Magnetic confinement fusion (MCF) research has largely focused on the design and optimisation of conventional aspect ratio tokamaks, but in parallel other configurations of devices including stellarators [1] and spherical tokamaks (STs) [2], have also been developed. These latter configurations could, in principle, obviate some of the engineering and more purely scientific challenges associated with delivering fusion energy from MCF devices.

STs offer several practical advantages including: radial compactness; potentially lower cost components; and improved plasma stability that allows operation at lower magnetic field compared to traditional tokamaks. Moreover, low aspect ratio and enhanced stability at high elongation gives STs access to operating regimes where a large fraction of the total plasma current is the self-driven bootstrap current. STs can operate at high  $\beta$  (where  $\beta$  is the ratio of plasma pressure to magnetic field energy density), and have achieved stable operation across a wide space in  $\kappa$  and  $\beta/l_i$  [3, 4], with energy confinement times that, while broadly consistent with multi-machine scaling laws, scale favourably with collisionality [5, 6].

The interest in STs has led to the construction of several machines in the past decades, including START [7], NSTX [8, 9], Pegasus [10], MAST [11], GLOBUS-M [12] and -M2 [13], MAST-U [14], ST40 [15], NSTX-U [16]. More recently, the UK has embarked on the STEP project to develop an ST-based fusion power plant (FPP) concept, with a major radius  $R \approx 3.6$  and an aspect ratio  $A \approx 1.8$ , with the goal of operating in a fully non-inductive regime and generating net electricity with a fusion power  $P_f \approx 1.5 GW$  [17]. The design of this reactor relies on experience gained from building and operating compact spherical tokamaks, such as MAST and MAST-U, that have found how challenges for STs differ from those facing conventional tokamaks.

Turbulence generally dominates transport in tokamaks, but the nature of this turbulence depends on plasma parameters and can therefore be extremely diverse. In particular, electromagnetic effects and magnetic fluctuations become more important at higher pressure gradient and at higher  $\beta$  values, that are more typically achieved in STs. Consequently it is to be expected that in STs, especially at high  $\beta$ , electrostatic turbulence will be supplemented

and potentially dominated by turbulence that is electromagnetic in character.

Magnetic fluctuations can have non-negligible transport implications, and often must be accounted for in the modelling of ST plasmas. In STs the turbulence is subject to stabilising effects arising from strong toroidicity reducing the impact of bad curvature, and relatively large  $E \times B$  shearing rates that act to de-correlate turbulent cells [18]. However, other kind of instabilities such as Kelvin–Helmholtz (KH) can destabilize the  $E \times B$  shear [19, 20, 21, 22] as it have been observed in gyrokinetic simulations of strongly rotating plasma in ST geometry configuration [23].

In STs it is often reported that the ion heat transport is close to neoclassical level [6] (although this is relatively large compared to high performing plasmas in conventional tokamaks) and that electron heat transport dominates the heat losses. For this reason the electron heat transport channels in STs from ETG and MTM turbulence have received particular attention [18, 24, 25, 26]. Nonlinear simulations of electromagnetic turbulence have proved more challenging computationally than for electrostatic turbulence, but a few such simulations studies have been performed for ST experiments and conceptual FFPs [26, 27, 28].

Microtearing instabilities, MTM, offer one mechanism that could be responsible for electron heat transport in STs, as these saturate at large amplitudes at the lower magnetic fields in spherical tokamaks. MTMs are electromagnetic instabilities, and resemble highwavenumber tearing modes [29], and are so-named because of the mode's characteristic breaking of equilibrium magnetic field lines to generate localized magnetic islands. There are several analytic theories of MTM instabilities in different regimes, but the drive mechanisms are less well validated against experiments than those associated with kinetic ballooning modes (KBM) or electrostatic instabilities. The analytic theories of MTMs generally apply in idealised regimes, and numerical investigations have proved essential for exploring this instability in the conditions of ST experimental plasmas. Gyrokinetic studies have demonstrated that microtearing instabilities can play significant roles not only in spherical, but also in conventional aspect ratio tokamaks [27, 29, 30, 31]. Moreover, gyrokinetic simulations show that MTM is unstable over a wide range of collisional regimes [32].

The saturation of MTM turbulence and dependencies on collisionality and temperature gradient have been studied numerically in [26, 28, 33]. Depending on local equilibrium conditions, microtearing mode turbulence can be sensitive [27] or insensitive to [30] equilibrium  $E \times B$  flow shear stabilisation effects, and this may be due to differences in magnetic shear [34, 35]. These subtle influences on the saturation of microtearing modes are probably related to a global stochastic behavior of the magnetic field lines, and have an important impact on the associated transport.

Reduced models for the core transport from MTM turbulence are required for integrated transport scenario modelling, but are not yet highly developed or validated against experiments. Previous transport simulations applying the reduced core transport model TGLF [36]‡ to MAST and NSTX discharges, underestimated the electron transport to varying degrees, indicating that other transport mechanisms may be playing an important role in electron heat transport [37].

In a recent extension of previous studies, transport simulations using the TGLF model and NEO for the neoclassical transport were found to be consistent with experimental data from two NSTX discharges dominated by electrostatic turbulence, one in L-mode and one in H-mode [38].

It is important to note that there is no exhaustive theory to describe turbulent diffusion of plasma in a stochastic magnetic field. This problem involves the interaction of different scales in turbulent transport and represents a very fascinating subject in plasma physics. In particular, transport in such an anisotropic medium requires the interplay of both longitudinal and transverse correlation mechanisms; an interplay that lies at the heart of the important model developed by Rechester and Rosenbluth (RR) to capture the essential physics [39, 40]. Other approximate theoretical and semi-theoretical models, such as those due to Rafiq [41, 42] and Rebut-Lallia-Watkins [43] respectively have been developed. A robust test of the stochastic transport models against a large common dataset would be highly desirable, but this does not vet exist.

To date these reduced stochastic models have been used to predict transport in a very modest number of ST discharges, and most publications have tested only a single model. Stochastic electron heat transport from MTM turbulence has been estimated for an NSTX discharge in Ref. [44], using an empirical modification of the RR model that includes an impact of the

density gradient. The role of density gradient is still not clear in stochastic theory applied to tokamaks. The normalised density gradient scale-length,  $R/L_n$ , is included in the RLW model, and gave reasonable matches to  $T_{exp}$  at radii and times where gyrokinetic calculations predict unstable MTMs [45] for NSTX shots. It has more recently been reported that including a model for stochastic transport from MTMs in the multimode model improves transport predictions for a high collisional NSTX discharge [42].

A high-fidelity reduced model for core transport from MTM turbulence is needed to complement models for other classes of turbulence. One of the main goals of this paper is to provide a more complete transport model for use in the integrated modeling tools widely used for tokamak scenario prediction, like JINTRAC [46] and ASTRA [47]. In this work we implement reduced models of stochastic field transport in JINTRAC, where these can be coupled with TGLF. Transport calculations with this more complete model are performed to predict equilibrium ion and electron temperature profiles. These predictions are then compared with measured profiles in the flat-top phase of experimental discharges from MAST/MAST-U.

The rest of this paper is structured as follows. In Sec. 2 we describe the physics basis of reduced models of stochastic transport, emphasizing main model assumptions and regimes of validity. Brief descriptions of the JINTRAC transport suite and the reduced transport model, TGLF, follow in Sec. 3 and Sec. 4, respectively. Then Sec. 5 describes the MAST/MAST-U discharges selected for transport analysis, and Sec. 6 compares transport model predictions for these discharges against the experimentally measured profiles. Finally the conclusions are developed in Sec. 7.

## 2. Stochastic models

Perturbations of the magnetic field can have a big impact on transport processes in tokamak devices, and affect the plasma equilibrium and its evolution. If the magnetic perturbations involve reconnection and are sufficiently strong, they destroy magnetic flux surfaces and can generate stochastic magnetic field regions. The locus of points at the intersection of the magnetic field with a poloidal cross-section of the plasma is no longer a smoothly defined curve belonging to a particular magnetic surface, but becomes an area-filling set of irregular random points. The magnetic field becomes stochastic at the surface q = m/n (where m and n are integer poloidal and toroidal mode numbers) when the adjacent width of the magnetic island,  $w_i$  given by:

$$w_i = 4\left(\frac{\delta B}{B_\theta} \frac{r}{n} \frac{1}{dq/dr}\right)^{1/2} \tag{1}$$

<sup>‡</sup> While the TGLF model includes magnetic fluctuations, the model was developed to describe turbulent transport from electrostatic turbulence, which dominates transport in the gyrokinetic simulations upon model is based. TGLF does not capture transport from MTM turbulence.

exceeds the distance between rational surfaces,  $\delta r_{res}$ :

$$\delta r_{res} = \frac{1}{ndq/dr} \tag{2}$$

The stochasticity condition,  $w_i > \delta r_{res}(r)$ , requires:

$$\frac{\delta B}{B_0} > \frac{1}{4^2} \frac{r}{R} \frac{1}{q^2} \frac{1}{ns} \tag{3}$$

where safety factor  $q \sim rB_0/RB_\theta$  and magnetic shear  $s = r/q \, dq/dr$ . The stochasticity threshold in Eq. 3 is exceeded at a critical mode amplitude that depends on toroidal mode number, safety factor, and magnetic shear. The relative amplitude of magnetic fluctuations,  $\delta B/B_0$ , increases with  $\beta$ , and this is often sufficiently large in STs to exceed the stochasticity threshold.

Different reduced models have been developed to describe stochasticity, though this is a complicated problem that is far from fully understood. The basic assumption is to consider an equilibrium magnetic field  $\mathbf{B_0}$  perturbed through a radial stochastic displacement  $\delta x$  in the direction perpendicular to  $\mathbf{B_0}$  corresponding to a magnetic field perturbation of amplitude  $\delta B$ . The equation of the perturbed field line relates  $\delta x$  to the parallel length,  $l_{||p}$ , of the perturbation in the  $\mathbf{B_0}$  direction:

$$\frac{\delta x}{l_{||p}} = \frac{\delta B}{B_0} \tag{4}$$

By assuming that  $l_{||p}$  length is traveled with a v velocity in a time  $\delta t = l_{||p}/v$  we can write for the diffusion coefficient along the perpendicular direction:

$$D_{eff} = \frac{\delta x^2}{\delta t} = \left(\frac{\delta B}{B_0}\right)^2 l_{||p} v = D_m v \tag{5}$$

where  $D_m$  is the magnetic diffusion coefficient that has the dimension of a length. The  $D_m$  coefficient provides a measure of the stochastic behavior of the magnetic field via the unknown longitudinal length scale  $l_{||p}$ . The quantity v in Eq. 5 is a characteristic velocity associated to the event. This velocity could be, for example, the velocity of an electron that moves along the magnetic field with a gyroradius equal to  $\rho_e$ . However, at the place to consider a single particle, it is important to generalize previous considerations via a statistical approach by considering a collective behavior of the plasma.

## 2.1. Kadomsev and Pogutse model

By considering collisional effects in the framework of a diffusive plasma, Kadomsev and Pogutse in Ref. [48] developed a model able to describe the stochastic dynamics establishing a relation between the perpendicular direction characterized by a collision decorrelation length and the parallel z direction with a  $D_{\parallel}$  diffusivity.

This model can be introduced by defining  $l_{\perp c}$  as the perpendicular displacement required for a particle to transfer to an uncorrelated field line. In the decorrelation time  $\delta t_{\perp}$  required for this transition, the particles diffuses along the longitudinal direction over a length  $l_{||} = \sqrt{D_{||}\delta t_{\perp}}$ .

Fig. 1 illustrates this mechanism whereby a particle trajectory transfers from one perturbed field line to an uncorrelated one when the perpendicular displacement from the initial field-line exceeds  $l_{\perp c}$ . The circle in Fig. 1 represents the Larmor orbit of an electron of radius  $\rho_e$ . In this model  $\rho_e = O(l_{\perp c}) \ll \Delta r$ , where  $\Delta r$  is the maximum separation between the distinct field lines. Defining a transverse diffusion

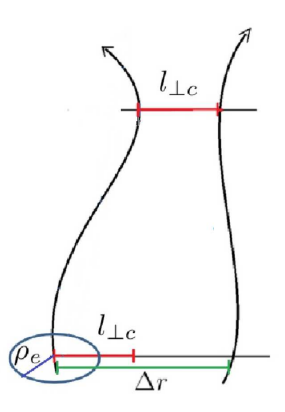


Figure 1. Stochastic perturbed magnetic field lines that approach each other at a decorrelation distance  $l_{\perp c}$  generally of the order of the electron Larmor radius  $\rho_e$  allowing an electron the possibility to jump from one line to another line via collisional process. The maximum distance between the magnetic field line is represented by  $\Delta r$ .

coefficient  $D_{\perp} = l_{\perp c}^2/\delta t_{\perp}$ , allows the decorrelation time to be expressed:

$$\delta t_{\perp} = \frac{l_{\perp c}^2}{D_{\perp}} \tag{6}$$

Substituting for the decorrelation time into the parallel diffusion equation,  $l_{||} = \sqrt{D_{||} \delta t_{\perp}}$ , gives:

$$l_{||} = \left(\frac{D_{||}}{D_{\perp}}\right)^{1/2} l_{\perp c} \tag{7}$$

Now the effective velocity of particles parallel to the magnetic field  $v = l_{||}/\delta t_{\perp}$ , can be expressed using (7) as:

$$v = \frac{\sqrt{D_{||}D_{\perp}}}{l_{\perp c}} \tag{8}$$

We can captures the collective diffusive process for a collisional plasma by substituting Eq. 8 into Eq. 5 to obtain:

$$D_{eff} = D_m v = D_m \frac{(D_{||} D_{\perp})^{1/2}}{l_{\perp c}} \tag{9}$$

This formula describes collisional particle motion in terms of diffusion both parallel and perpendicular to the perturbed field, and particles transfer to uncorrelated field lines when the perpendicular displacement exceeds  $l_{\perp c}$ ; this dynamics gives rise to anomalous transport in the radial direction. The model is "collisional" in the sense that the perpendicular displacement of particles, between distinct magnetic field lines, is assumed to be completely due to collisional processes. However, collisional transport is not the only process that can decorrelate particles from magnetic field lines.

## 2.2. Rechester-Rosenbluth model

In the same year as [48], Rechester and Rosenbluth described an alternative more efficient decorrelation mechanism [39, 40]. RR highlighted that in a stochastic field, two neighboring magnetic field lines separated by a perpendicular distance  $x_d$ , at one location, become exponentially separated on advancing in the direction of the magnetic field; i.e. the separation between particles, x(t), following field-lines initially separated by  $x_d$ , increases with the parallel displacement z(t) according to:

$$x(t) = x_d e^{z(t)/l_K} (10)$$

where  $l_K$ , the Kolmogorov length scale, is an important parameter characterizing the chaotic motion of the magnetic field. This scale contains "information" associated with the trajectories of the system, and is related to the dynamic entropy [49, 50]. Kolmogorov statistical approach is adopted and extended by RR to a deterministic stochastically unstable system in which  $l_K$  is determined also from the geometrical configuration of the magnetic field; in tokamaks the field geometry is characterised by the magnetic shear, which changes in the radial direction. In the Rechester-Rosenbluth mechanism the decorrelation of the magnetic field experienced by a particle, arises primarily because of the divergence of the magnetic field lines, with collisions playing a modest but yet essential role in seeding the process.

Consider field lines passing through a small circular area  $A=\pi x_d^2$  of radius  $x_d$  in the poloidal plane of a tokamak plasma. The fields passing through the circle at z=0 diverge and the outer radius of the locus of the field lines increases as  $x(z)=x_d e^{z/l_K}$  from Eq. 10. From conservation of magnetic flux it follows that as the fields expand, this locus must also develop increasingly fine scale dendritic structures (of width  $\delta \sim x_d e^{-z/l_K}$ ) in the perpendicular plane as z increases. We apply this argument to field lines bounded at z=0 by a circle of radius  $l_{\perp c}$ , where  $l_{\perp c}$  characterises the field decorrelation distance, to find

that the separation between uncorrelated fields,  $r_c(z)$ , narrows with z as:

$$r_c(z) = l_{\perp c} e^{-z/l_K} \tag{11}$$

Assuming collisional particle trajectories governed by parallel and perpendicular diffusion:

$$r = \sqrt{D_{\perp}t} \qquad z = \sqrt{D_{\parallel}t} \tag{12}$$

it follows that:

$$r = \sqrt{\frac{D_{\perp}}{D_{\parallel}}} z \tag{13}$$

In the limit where stochasticity plays no role, i.e.  $l_K = \infty$ , the decorrelation length  $l_{\perp c}$  is accessed through collisions alone. Setting  $r(l_{\parallel c}) = l_{\perp c}$  using Eqn.13 directly gives the Kadomtsev and Pogutse result of Eq.6,  $l_{\parallel c} = l_{\perp c} \sqrt{D_{\parallel}/D_{\perp}}$  [51].

Now let's consider an element of plasma of perpendicular thickness  $\delta$  in a stochastic magnetic field. The collisional particle trajectories are governed by Eq.13, and follow correlated fields described in Eq. 11. At increasing z the element thickness,  $\delta$ , of the correlated plasma is simultaneously subjected to narrowing by stochasticity and to expansion from particle collisions, so that:

$$\frac{d\delta}{dz} = -\frac{\delta}{l_K} + \sqrt{\frac{D_\perp}{D_\parallel}}. (14)$$

The typical thickness of this correlated region of plasma is estimated from when these opposing influences balance; i.e. when  $\frac{d\delta}{dz} = 0$  at:

$$\delta = l_K \sqrt{\frac{D_\perp}{D_\parallel}} \tag{15}$$

Now  $\delta = r_c(l_{\parallel c})$ , so we obtain the parallel correlation length  $l_{\parallel c}$  by combining Eq.11 and Eq. 15 to give:

$$l_{\parallel c} = l_K \ln \left[ \frac{l_{\perp c}}{l_K} \sqrt{\frac{D_{\parallel}}{D_{\perp}}} \right]$$
 (16)

This gives all the information required to determine the stochastic diffusion coefficient from Eq. 5. The characteristic velocity,  $v = D_{\parallel}/l_{\parallel c}$  arises from parallel diffusion (and is obtained using  $v = l_{\parallel c}/\delta t$  together with  $D_{\parallel} = l_{\parallel c}^2/\delta t$ ). From Eq. 5 we have:

$$D_{eff} = D_m v = \left(\frac{\delta B}{B}\right)^2 \frac{l_{\parallel p}}{l_{\parallel c}} D_{\parallel} \tag{17}$$

Substituting Eq. 16 into Eq. 17 gives the general expression for the RR model transport diffusivity. In Sec.3.1 Eq. 17 will be used as the basis of RR-based models in collisional and collisionless limits in JETTO.

The RR model establishes different scales that are fundamental to stochastic transport (e.g.  $l_{\parallel c}$ ,  $l_{\perp c}$   $l_{\parallel p}$ , and  $l_K$ ) but does not quantify all of them, which is the

price paid for the RR model's simplified description of stochastic transport. Appropriate models are needed to independently estimate these scales from the characteristics of the plasma configuration, and this represents the main difficulty in exploiting the model.

### 2.3. Rebut-Lallia-Watkins model

As discussed in Sec. 2, if magnetic islands are sufficiently large to overlap they generate stochastic, or ergodic, magnetic field regions. The Rebut-Lallia-Watkins (RLW) model [43] is a semi-empirical description of plasma transport under such conditions, and its model predictions have been compared with measured profiles from an NSTX H-mode plasma [45].

The RLW model is based on dimensionless plasma parameters, and was first developed to predict plasma profiles in ohmic and L-mode JET discharges by exploiting an analogy between fluid and plasma turbulence. In fluids the dimensionless Reynolds number  $R_e$ , which characterizes the relative importance of momentum transport by convection and by viscous diffusion, allows to fix the transition from the laminar to the turbulence regime when  $R_e$  exceeds a critical value,  $R_{e,c}$ . The corresponding change in radial heat and particle flows observed in fluids is also observed in tokamaks by considering this latter as an open thermodynamic system in which heat flow could influence its stability. Thus, the RLW model determines a critical temperature gradient  $|\nabla T_e|_c$  for a plasma, equivalent to a critical Reynolds number to define the development of turbulence due to a stochastic instability in a tokamak:

$$|\nabla T_e|_c = \left| \frac{dT_e}{dr} \right|_c = 0.06 \frac{e}{(\mu_0 m_e^{0.5})^{0.5}} \frac{1}{q} \left( \frac{\eta J B^3}{n_e T_e^{0.5}} \right)^{0.5} \tag{18}$$

where  $\eta$  is the Spitzer resistivity and J is the current density. When the electron temperature gradient exceeds  $|\nabla T_e|_c$  the electron transport becomes:

$$\chi_{RLW} = 0.5c^2 \sqrt{\mu_0 m_i} \frac{(1 - \sqrt{r/R})}{BR^{0.5}} \left(\frac{T_e}{T_i}\right)^{0.5}$$

$$\left(\frac{1}{T_e} \frac{dT_e}{dr} + 2\frac{1}{n_e} \frac{dn_e}{dr}\right) \frac{q^2}{dq/dr}$$

$$\sqrt{1 + Z_{\text{eff}}} \left(1 - \frac{|\nabla T_e|_c}{|\nabla T_e|}\right)$$

$$H(|\nabla T_e| - |\nabla T_e|_c)$$
(19)

where the Heaviside functions, denoted H(..), trigger anomalous transport above the critical electron temperature gradient in regions with dq/dr > 0. Moreover, if dq/dr changes in sign from positive to negative value,  $\chi_{RLW}$  becomes zero. The RLW model is also sensitive to the density gradient; indeed while the model only triggers transport above a

threshold in  $\nabla T_e$ , the ensuing transport is twice as sensitive to the logarithmic density gradient as to the logarithmic electron temperature gradient. (This transport sensitivity to density gradient is not present in the RR models of stochastic transport discussed above.) Although the modelled microtearing transport level in Eq. 19 is strongly dependent on  $n_e$ ,  $T_e$ ,  $T_i$ , q, and their gradients, there is no clear dependence on either collisionality or  $\beta_e$  which should also influence microtearing-induced transport. Some of these dependences are implicitly in the critical gradient of Eq. 18, but this has virtually no effect on transport when the temperature gradient exceeds the critical threshold across the radial cross-section (as for the NSTX shot analysed in [45]). §

All of the models for stochastic field transport described in Section 2 have been implemented in the integrated modelling tool JINTRAC. Transport calculations using these stochastic transport models, together with models like TGLF to describe the transport from electrostatic turbulence, to test and validate these models against experimental data from MAST and MAST-U, will be reported in Section 6.

## 3. JINTRAC code

JINTRAC [46] is a popular transport simulation tool used by the fusion community to model and optimize tokamak plasma scenarios, and to make predictions for future devices. It incorporates a wide range of physics-modules to model different aspects of the tokamak plasma discharge, and the various modules can be selected and configured via a convenient bespoke JAMS interface. This is extremely flexible and facilitates a wide range of simulations with different levels of complexity and fidelity.

Here we exploit JETTO, the core transport solver at the heart of JINTRAC, to model the transport evolution of fixed-boundary plasma equilibria. JETTO solves the plasma fluid transport equations for quantities that are averaged over magnetic surfaces ||, and requires the 2D plasma equilibrium for a prescribed boundary in the poloidal plane. The 2D equilibrium is either computed self-consistently using JINTRAC's internal equilibrium module ESCO, or taken from an external calculation (e.g. by EFIT or CREATE). JETTO can be used to model a wide variety of tokamak transport problems of interest.

 $\S$  RLW model predicted  $T_e$  profiles were reported in [45] to be in good agreement with measurements from an NSTX discharge at times when gyrokinetic simulations revealed MTMs to be unstable and dominant, but less well for times when MTMs were stable or sub-dominant.

 $\parallel$  JETTO solves 1D transport equations for the plasma radial profiles together with a 2D equilibrium equation, following the standard 1.5D approach to model transport in tokamaks.

The transport matrix contains the various contributions to the fluxes of heat and particles, and its coefficients must be calculated for each species. This contains contributions from both neoclassical and anomalous transport. The neoclassical transport contribution is calculated independently using the NCLASS module and this is added to the anomalous transport. Calculation of the various transport coefficients requires as inputs: density, temperature, momentum and the gradients of these quantities for electrons and all ion species, and the Grad-Shafranov equilibrium (which includes the magnetic shear and q profiles). The transport models are computed within JETTO at each time step to obtain the transport matrix, and the profiles are evolved forwards in time by inverting a matrix equation using the Transport Code Interface, TCI, [52].

The following anomalous transport models are available in JETTO and will be used in this paper's simulations: Bohm/gyroBohm [72] and TGLF [36, 53, 54]. In this paper we will additionally include the RR and RLW models of transport from stochastic magnetic fields, and we will specify regions of validity for the RR models.

## 3.1. Implementation of the reduced stochastic models in JINTRAC

In order to implement stochastic models in JINTRAC, different assumptions and approximations have been done. For convenience we rewrite Eq. ?? to make the magnetic diffusivity dependence on  $\delta B/B_0$  explicit:

$$D_{eff} = D_m \frac{D_{||}}{l_{||c}} = \left(\frac{\delta B}{B_0}\right)^2 l_{||p} \frac{D_{||}}{l_{||c}} \tag{20}$$

Nonlinear drift-kinetic theory of the stochastic turbulence suggests saturation occurs at amplitude [55]

$$\frac{\delta B}{B} = \frac{\rho_e}{L_T} \tag{21}$$

where  $\rho_e$  is the thermal electron gyroradius and  $L_T$  is the electron temperature gradient scale length. Eq. 21 has been obtained in Ref. [55] in the framework of a drift-kinetic theory. While gyrokinetic simulations of MTM turbulence performed with GENE at conventional aspect ratio [30, 56] and with GYRO and CGYRO for STs [33, 26], are broadly consistent with Eq. 21 across a range of parameters,  $\delta B/B$  is also strongly sensitive to other plasma parameters including  $\beta_e$ ,  $\nu_{ei}$ , flow shear, and other equilibrium quantities [33, 26]. There are several possible approaches to improve on  $\delta B/B$  from Eq. 21:

- more detailed reduced models for  $\delta B/B$  may emerge from nonlinear gyrokinetic simulations;
- Rafiq's reduced model of stochastic transport from MTMs [41] estimates  $\delta B/B$  from a nonlinear dispersion relation in simplified geometry that is independent of Eq. 21;

• the TGLF model can provide an estimate of  $\delta B/B$  (though TGLF does not reliably capture MTMs).

In future work we will compare alternative approaches to modelling  $\delta B/B$ . Length-scale parameters  $l_{||p}$  and  $l_{||c}$  are also required in Eq. 20. We assume  $l_{||p}$  to be of the order of the major radius, R, of the tokamak [27, 44], and estimate  $l_{||c}$  from experimental conditions using the analytic formula of Eq. 27 as discussed in Sec.6. Thermal conduction coefficients come from kinetic theory, which gives  $D_{||}^{e,i} \sim \chi_{||}^{e,i} \propto T_{e,i}\tau_{e,i}/m_e$  where  $\tau_{e,i}$  is the electron/ion collision time, and  $D_{\perp}^{e,i} \sim \chi_{\perp}^{e,i} \propto T_{e,i}/m_{e,i}\omega_{e,i}^2\tau_{e,i}$  where  $\omega_{e,i}$  is the electron/ion gyrofrequency for species e,i along parallel and perpendicular direction respectively. Results of the kinetic theory on the thermal conduction coefficients allow to have  $D_{||}^{e,i} \sim \chi_{||}^{e,i} \propto T_{e,i}/m_e$  and  $D_{\perp}^{e,i} \sim \chi_{\perp}^{e,i} \propto T_{e,i}/(m_{e,i}\omega_{e,i}^2\tau_{e,i})$  for species e,i along parallel and perpendicular direction respectively. Thus, we can write for electrons:

$$D_{||}^{e} \sim \chi_{||}^{e} = 3.16 \frac{T_e \tau_e}{m_e} \sim v_e^2 \tau_{ei} \sim \frac{v_e^2}{\nu_{ei}}$$
 (22)

We assume the following expression for the electron-ion collision time:

$$\tau_{ei} = 2\pi \frac{\epsilon_0^2 m_e^{0.5} (k_B T_e)^{3/2}}{Z_{eff}^2 n_i e^4 \ln \Lambda}$$
 (23)

where  $\epsilon_0$  is the electric susceptibility and  $\ln \Lambda$  is the Coulomb logarithm. By observing that  $v_e^2 \tau_{ei} \sim v_e^2/\nu_{ei} \sim v_e \lambda_{mfp}$ , Eq. 20 becomes:

$$\chi_e \approx \left(\frac{\rho_e}{L_{T_e}}\right)^2 R v_e \frac{\lambda_{mfp}}{l_{||c}} \tag{24}$$

This equation has been adopted as collisional model of the RR theory. In Ref. [39] it is emphasized that Eq. 24 works well when  $l_{||c} > \lambda_{mfp}$ . Then, Eq. 24 predicts a transport that is more or less  $\lambda_{mfp}/l_{||c}$  time than that one of the collisionless regimes. For collisionless model we have:

$$\chi_e \approx \left(\frac{\rho_e}{L_T}\right)^2 R v_e 2 \sqrt{\frac{2}{\pi}} \left(1 - \sqrt{\frac{r}{R}}\right)$$
(25)

where the last right term is a parameter related to the fraction of passing particles [57, 58]. The adoption of  $f_p$  is also supported by gyrokinetic simulations devoted to investigate stochastic regime [59]. It is interesting to observe that the RR model has not a density gradient dependence, where the RLW model presents a factor two in front to the density gradient dependence with respect to  $\nabla T_e$ .

Concerning the RLW model, in JETTO the Heaviside function of temperature gradient that appears in the RLW heat diffusivity of Eq. 19, is replaced with:

$$H(|\nabla T_e| - |\nabla T_e|_c) = \frac{1}{2} \left[ \tanh \left( \frac{|\nabla T_e(r)|}{b|\nabla T_e(r)|_c} - \frac{a}{b} \right) + 1 \right] (26)$$

where a=0.9 and b=0.01 are parameters in a hyperbolic tangent representation of the Heaviside function that regulate the position of the critical gradient and its steepness on threshold. This smoothed representation improves numerical stability with respect to discontinuous changes in time of transport close to threshold.

## 4. TGLF code

The trapped-gyro-Landau-fluid (TGLF) code is a firstprinciples-based quasi-linear reduced core transport model that was developed to describe anomalous transport from predominantly electrostatic turbulence. TGLF solves linearised gyrofluid equations that account for kinetic effects including Landau damping, gyro-averaging, electron-ion collisions, impurities, trapping and other toroidal geometry effects. TGLF describes turbulent transport from various classes of microinstabilities including ion temperature gradient modes (ITG), electron temperature gradient modes (ETG), and trapped electron modes (TEM). TGLF calculates magnetic fluctuations so can also compute the linear properties of electromagnetic modes like kinetic ballooning modes (KBMs) and Alfvénic ITG modes, that may be important for transport in higher  $\beta$  regimes. Physics properties of the dominant linear eigenmodes are calculated by TGLF's gyro-fluid solver, and this is supplemented by saturation rules to set the model transport fluxes. These saturation rules were tuned to fit turbulent fluxes from databases of nonlinear gyrokinetic simulations across a wide range of plasma conditions. Several different saturation rules have been developed and released as this database has expanded: SAT0 [60], SAT1 [61], SAT2 [62], and SAT3 [63].

While TGLF captures some electromagnetic modes linearly, its saturation models (which is obviously critical to transport prediction) are tuned to gyrokinetic simulations of predominantly electrostatic turbulence. TGLF has been used routinely to model anomalous transport in conventional aspect ratio tokamaks like JET and DIII-D, including high  $\beta_p$  steady state plasma scenarios [65, 66, 67].

TGLF can describe transport contributions from electrostatic turbulence in spherical tokamaks, and there have been several comparisons of TGLF predictions against data from ST discharges [68, 38]. We note that first transport simulations for NSTX [38] using NEO for the neoclassical fluxes together with TGLF(SAT1) are found to be more stable than those using those using NEO with TGLF(SAT2), and that TGLF(SAT2) simulations for an NSTX H-mode were found to over-predict the contribution of low-k modes to the total turbulent flux whilst

those using TGLF(SAT1) were consistent with power balance analysis [38]. A key limitation of TGLF, however, is that it does not include stochastic field transport generated by microinstabilities like MTMs. This is addressed here by supplementing TGLF with other models to describe the missing transport from stochastic magnetic fields. In this work TGLF is mainly run with the SAT1 and SAT2 saturation rules \( \bigvert, and the anomalous fluxes are supplemented using the reduced models of stochastic field transport described in section 2.

## 5. Experimental data selection and data analysis

In this work stochastic models have been supplemented with TGLF, for the first time, to make transport predictions for MAST and MAST-U plasmas. This section discusses the selection of shots for this analysis. Key parameters for MAST and MAST-U are: major radius R = 0.85m, minor radius a = 0.65m, plasma current  $I_{p_M},I_{p_{MU}}\leq 1.3,2\text{MA},$  magnetic field  $B_M,B_{MU}\leq 0.52,0.75\text{T}$  and pulse length  $T_{p_M},T_{p_{MU}}\leq$ 0.6, 5s. Where quantities differ between these devices, these are distinguished using the subscripts M and Longer pulse lengths should give MAST-U longer and steadier flat-top phases than were accessible in MAST. We also note that at constant pressure, the lower magnetic field in MAST increases  $\beta$  and the likely impacts of transport from stochastic fields. Transport analysis and model validation is more robust when it is applied using data to steady state shots with optimal stability conditions. This first analysis focuses on a small number of such discharges, but after verifying this approach it can be extended to a broader database of discharges in future work. We have selected experimental discharges, where the variation in time on temperature and density at  $\rho_n = 0.5$  in the middle of the radial domain (which we label g) is characterized by  $G = 1/g(dg/dt) < 3s^{-1}$ . We have applied this selection criterion to high fidelity interpretive TRANSP simulations from MAST and MAST-U to find the most suitable discharges that are analysed in this paper. Four discharges that survive these selection criteria will be used in this paper at particular times, and these are: #22664, #22769 from MAST; and #46978, #47003 from MAST-U. We have also required that thermal transport is not strongly affected by Magnetohydrodynamic (MHD) instabilities in the period of interest. To illustrate this, Fig. 2 shows the time evolution of  $\frac{1}{q} \frac{dg}{dt}$  for MAST-U#47003, and Fig. 3

¶ SAT1, described in [61], replaces flow shear quench rule of SAT0 [60] with a spectral shift model and accommodates findings from the first multi-scale gyrokinetic simulations, while SAT2 [62] refines SAT1 to accommodate more detailed analysis of spectra from nonlinear GK simulations.

shows the corresponding profile measurements and the TRANSP fits that were used. In particular, figure shows profiles of electron temperature (red color), ion temperature (blue color) and density (green color) at t=0.451s. In the same way, Fig. 4, Fig. 5 and Fig. 6 show profile comparison between experiments and TRANSP fits for shots #46978 MAST-U at t=0.615s, #22664 MAST at t=0.23s and #22769 MAST at t=0.23s respectively.

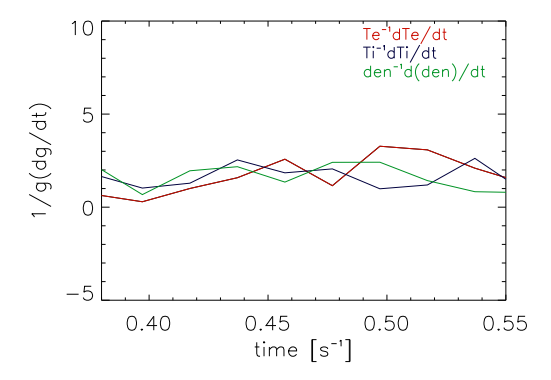


Figure 2. Time evolution of G=1/g(dg/dt) quantity that represents the average along the radial domain for electron (red), ion (blue) temperature and density (green) profiles for the MAST-U case 47003.

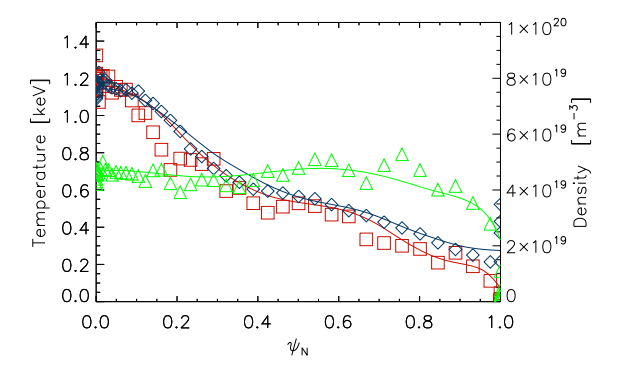


Figure 3. Comparison of density (green), electron (red), ion (blue) temperature profiles between experimentals and interpretative TRANSP fit at the selected time t=0.451s in the flat-top phase for the MAST-U case #47003.

The radial profiles have been measured by using different diagnostic systems. The electron plasma temperature and electron density have been obtained using the Thomson scattering system, which measures from the high field side to the low field side, along the

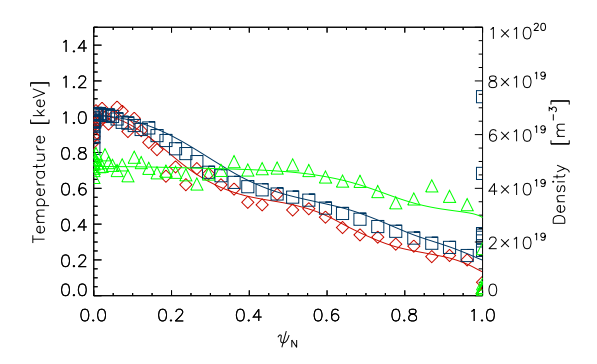


Figure 4. Comparison of density (green), electron (red), ion (blue) temperature profiles between experimentals and interpretative TRANSP fit at the selected time t=0.615s in the flat-top phase for the MAST-U case #46978.

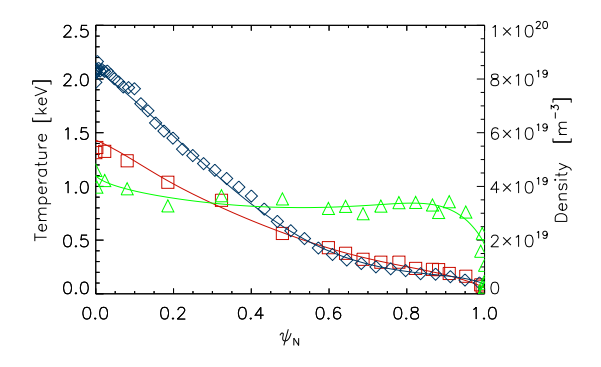


Figure 5. Comparison of density (green), electron (red), ion (blue) temperature profiles between experimentals and interpretative TRANSP fit at the selected time t=0.23s in the flat-top phase for the MAST-U case #22664

plasma midplane. The toroidal rotation profiles have been determined by Charge Exchange Recombination Spectroscopy, and the impurity concentration was estimated by the effective plasma charge  $(Z_{eff})$ . Radiated power profiles have been measured by the bolometer diagnostic.

All the kinetic and MHD equilibrium reconstruction have been obtained through running TRANSP and EFIT integrated workflows using the OMFIT framework. The magnetic equilibrium configurations are shown in Fig. 7, where from left to right there is a clear gradual increase in the elongation from  $\kappa=1.73$  to  $\kappa=2.15$ . Safety factor profiles are plotted in Fig. 8. In all selected shots, the minimum safety factor q is above unity and no sawtooth activity has been detected. For these cases no kinks, fishbones, or tearing

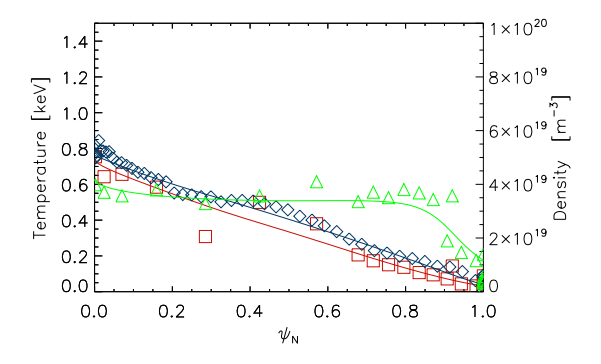
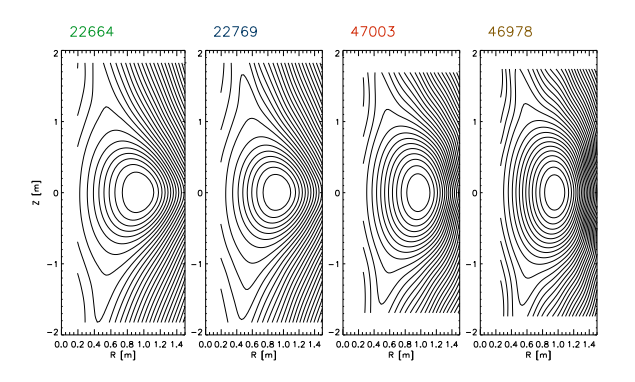
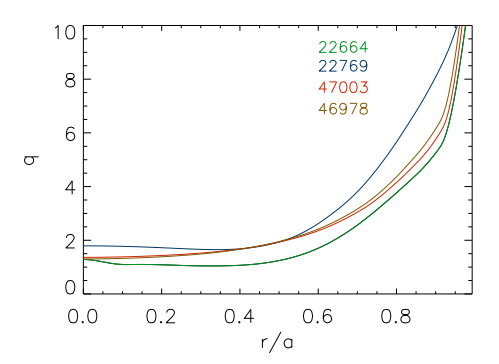


Figure 6. Comparison of density (green), electron (red), ion (blue) temperature profiles between experimentals and interpretative TRANSP fit at the selected time t=0.2s in the flat-top phase for the MAST-U case #22769



**Figure 7.** Magnetic configuration for MAST cases 22664 (t=0.23s) and 22769 (t=0.2s) and MAST-U cases 47003 (t=0.451s) and 46978 (t=0.615s). It is possible to appreciate the change in elongation for the different cases.



**Figure 8.** Safety factor profiles for MAST cases 22664 (t = 0.23s) and 22769 (t = 0.2s) and MAST-U cases 47003 (t = 0.451s) and 46978 (t = 0.615s).

modes have been detected in the neutron rate or by the Mirnov coils signals.

Values of elongation and q are reported in Table 1 together with the other main plasma parameters such as plasma current  $I_p$ , vacuum toroidal magnetic field on axis  $B_0$ , inverse aspect ratio etc.

The MAST discharges are in L-mode and were produced as part of a collisional scan to test the sensitivity of confinement, and they have been discussed in [5]. These latter together with MAST-U cases have been selected with the goal to explore a certain range of collisionality that represents a good parameter value for the applicability of the stochastic model. The MAST-U cases are in *H*-mode regime.

### 6. Results

Here we describe results of JINTRAC calculations using a variety of stochastic transport models to supplement TGLF (using SAT1 and SAT2) in the JETTO transport solver. Simulations have been performed for the prediction of electron and ion temperature profiles,  $T_e$  and  $T_i$ , with density and rotation set to fit the experimentally measured profiles, and impurity density profiles estimated using the measured  $Z_{eff}$ . Our simulations have additionally required as inputs the magnetic equilibrium configuration, and temperatures at the boundary point fixed at r/a = 0.9. Table 2 gives the characteristic mid-radius values of some key plasma parameters from each discharge.

The selected shots span a range in collisionality (indeed the selected MAST discharges are from the extremes of the collisional scan described in [5]), which, as discussed earlier, is an important parameter in the transport processes from stochastic fields.

To make an initial assessment of the possible importance of radial stochastic transport, we can compare magnetic island width,  $w_i$ , estimated using Eq. 1 for a given toroidal mode number, n, with the distance between rational surfaces,  $\delta r_{\rm res}$ , from Eq. 2. This comparison also requires knowing the amplitude of the magnetic fluctuation, which can be estimated using the Drake ansatz of Eq. 21. Fig. 9 shows this comparison for #22664 for n=6 and n=16. We observe that around  $r \approx 0.4$  for toroidal number n = 6 (red line), the quantity  $w_i$  becomes larger than  $\delta r_{res}$  and consequently we expect that stochastic process could become important. By increasing n value the threshold stochastic condition shifts toward lower values of r, as shown in Fig. 9 for n = 16 (blue line). This behaviour is typical in the MAST/MAST-U discarges we have analysed.

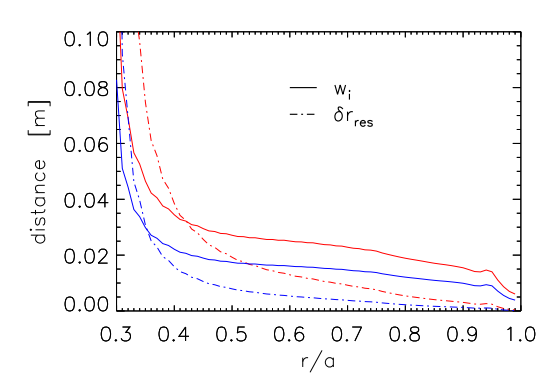
The ratio between  $w_i$  and  $\delta r_{res}$  is a good approximation of the so called stochastic parameter. This parameter have been introduced in Ref. [64] and

Table 1. Values of parameters for the MAST shot 22664, 22769 (L-mode) and MAST-U shots 47003, 46978 (H-mode). We report
the following quantities: current $I_p$ , vacuum toroidal magnetic field at geometric axis $B_0$ , Mach number $M$ , auxiliary power $P_{NBI}$
from NBI, $q_{95}$ , $Z_{eff}$ , $\beta = n(Te + Ti)/[B_0^2/(2\mu_0)]$ , elongation $\kappa$ and inverse aspect ratio $\epsilon = a/R$ .

S	Shot num	$I_p(kA)$	$B_0(T)$	M	$P_{NBI}$	$q_{95}$	$Z_{eff}$	$\beta$	$\kappa$	$\epsilon$
	22664	886	0.50	0.35	3.2	7.2	1.3	0.067	1.73	0.71
	22769	592	0.34	0.32	3.0	9.6	1.3	0.094	1.80	0.7
	47003	730	0.66	0.19	1.3	7.8	1.5	0.051	2.00	0.81
	46978	750	0.60	0.25	3.0	8.5	1.5	0.060	2.15	0.75

Table 2. Values of parameters for the MAST shots 22664, 22769 (L-mode) and MAST-U shots 47003, 46978 (H-mode) All the value have been calculated in the middle of the radial domain. We report electron  $T_e$  and ion  $T_i$  temperatures, density  $n_e$ , ion  $\rho_i$  and electron  $\rho_e$  Larmor radius, mean free path  $\lambda_{mfp}$ , electron-ion collisional frequency  $\nu_{ei}$ , longitudinal decorrelation scale  $l_{||c}$ .

Shot	$T_e$ [eV]	$T_i$ [eV]	$n_e(10^{19}m^{-3})$	$\rho_i$ [m]	$\rho_e$ $[m]$	$\langle \lambda_{mfp} \rangle [m]$	$\langle \nu_{ei} \rangle \ [s^{-1}]$	$\langle l_{  c} \rangle \ [m]$
22664	600.0	683.3	3.2	$1.1\cdot 10^{-2}$	$1.6\cdot 10^{-4}$	8.39	$1.90\cdot 10^6$	2.18
22769	361.6	438.5	3.4	$1.3\cdot 10^{-2}$	$1.9\cdot 10^{-4}$	3.07	$4.02\cdot 10^6$	2.89
47003	570.1	616.0	4.7	$7.7\cdot10^{-3}$	$1.2\cdot 10^{-4}$	6.78	$2.10\cdot 10^6$	4.19
46978	541.8	595.0	4.64	$8.3\cdot10^{-3}$	$1.3\cdot 10^{-4}$	5.81	$2.33 \cdot 10^{6}$	2.86



**Figure 9.** Comparison between magnetic island  $w_i$  and distance between rational surfaces  $\delta r_{res}$  for n=6 (red lines) and n=16 (blue lines). The curves referred to the 22664 MAST case.

could be used to give an estimation of  $l_{||c|}$  quantity via the following analytical expression:

$$l_{||c} \approx \frac{\pi R}{\ln\left[\pi w_i/(2\delta r_{res})\right]} \tag{27}$$

It is important to note that Eq. 27 has been derived for one single n mode [39]. The general espression for

a complete spectrum of n is unknown. However, we expect for this case, a value of  $l_{||c|}$  lower than that one obtained in Eq. 27. In this paper for MAST/MAST-U we always use n = 16 to compute  $l_{\parallel c}$ , because this is the principal toroidal wave number that emerges in gyrokinetic simulations of MTM turbulence in MAST discharges [26]. It is important to point out that  $l_{\parallel c}$ is only weakly sensitive to this choice of n because of the logarithmic dependence in Eq. 27. To identify the most appropriate reduced stochastic transport model, it is important to consider the collisional regime that is relevant to the experimental conditions. In Fig. 10, we compare the mean free path  $\lambda_{mfp}$  and the  $l_{||c}$ value calculated in the middle of the radial domain, for each of the four discharges. Both quantities are plotted as a function of the mid-radius collisionality  $\nu_{ei}$ , which varies across the discharges, and Fig. 11 compares radial averages  $\langle \lambda_{mfp} \rangle$  and  $\langle l_{||c} \rangle$  as functions of  $\langle \nu_{ei} \rangle$ , where the average is performed over the region 0.45 < r/a < 0.75.

Fig. 10 and Fig. 11 clearly demonstrate that  $\lambda_{mfp} > l_{||c}$  in the lowest collisional MAST discharge #22664, and that this criterion is also satisfied less strongly in MAST-U discharges #47003 and #46978. Satisfying  $\lambda_{mfp} > l_{||c}$  indicates that the more suitable RR stochastic model for these discharges will be the

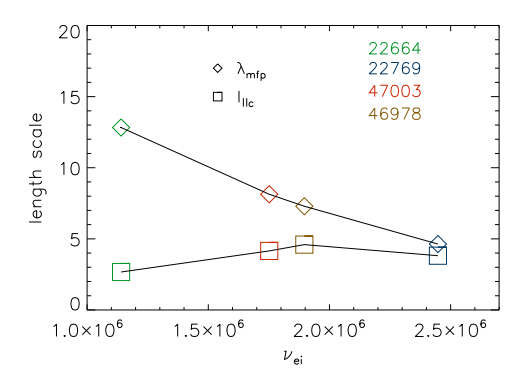


Figure 10. Mean free path  $\lambda_{mfp}$  and  $l_{||c}$  parameters expressed in meters [m] as a function of collisionality  $\nu_{ei}$  in  $[s^{-1}]$ .

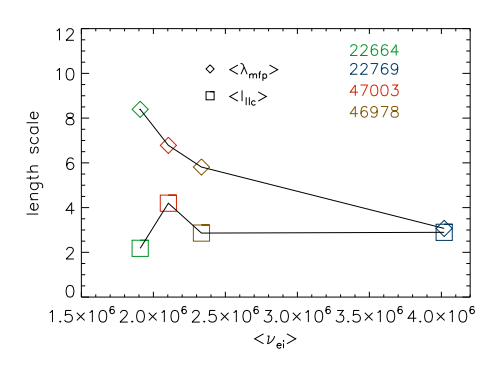
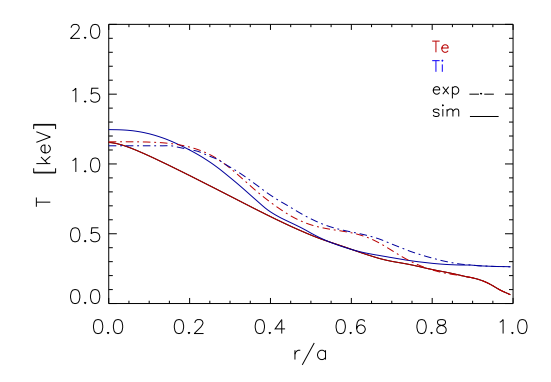


Figure 11. Average mean free path  $\langle \lambda_{mfp} \rangle$  and average  $\langle l_{||c} \rangle$  parameters expressed in meters [m] as a function of the average collisionality  $\langle \nu_{ei} \rangle$  in  $[s^{-1}]$ . Quantities are averaged between r=0.45a and r=0.75a.

"collisionless" model (see Sec. 3.1). Identifying the appropriate RR collisional regime is more ambiguous for MAST #22769 where  $\lambda_{mfp} \approx l_{||c}$ . The RR-collisionless RR<sub>c-less</sub> model has been used in JETTO together with either TGLF(SAT1) or TGLF(SAT2).

Thus, we first report transport simulations for the MAST-U H-mode #47003, using the  $RR_{c-less}$  model and TGLF(SAT1) excluding further effects from magnetic fluctuations (TGLF(SAT1)ES). The top panel of Fig. 12 compares  $T_e$  and  $T_i$  experimental profiles (dash-dotted lines) with the transport steady state profile predictions (continuous lines). The bottom panel shows the total electron and ion thermal diffusivities,  $\chi_e$  and  $\chi_i$ , together with their respective contributions from the  $RR_{c-less}$  model, and from ion neoclassical heat transport,  $\chi_{i_{neo}}$ . Ion heat



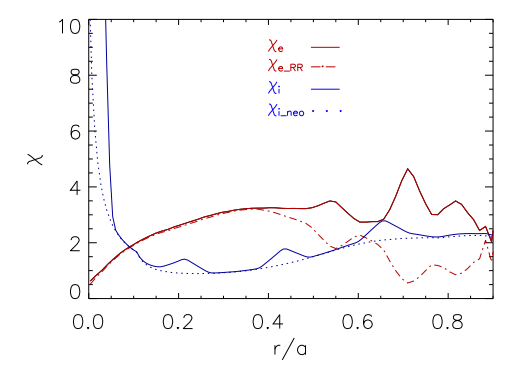
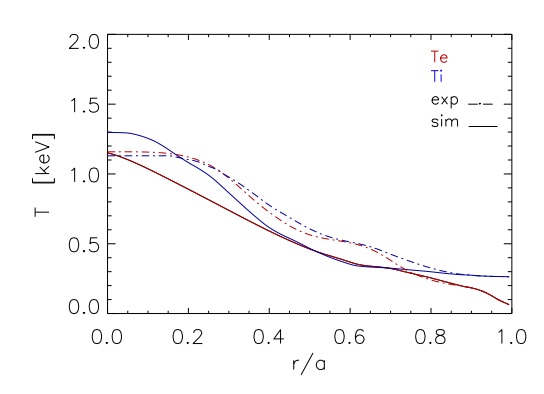


Figure 12. (Top panel) Experimental data (dash-dotted line) of ion and electron temperature profiles compared with simulation profiles (continuous lines) for the MAST-U case 47003 in electrostatic transport model . (Bottom panel) Associated total ion and electron diffusion coefficient  $\chi_i$  and  $\chi_e$  in blue and red continuous lines respectively. Rechester-Rosenbluth  $\chi_{RR}$  and neoclassical diffusion  $\chi_{i_{neo}}$  coefficients in red dashed and blue dotted lines respectively. Diffusion coefficients are expressed in  $[m^2/s]$ .

transport is entirely dominated by the neoclassical term #47003, while electron heat transport is dominated by stochasticity, in particular in the central box around r=0.4 with the peak electron heat diffusivity  $\chi_e \sim \chi_{eRR} \sim 3m^2/s$ .

Modelling the same discharge including electromagnetic effects in TGLF (RR<sub>c-less</sub>+TGLF(SAT1)EM) gives the similar temperature profile predictions illustrated in the top panel of Fig. 13. The bottom panel shows that the small change in profiles is due to the presence of enhanced ion transport between 0.6 < r < 0.8, and comparison with Fig. 12 indicates that this can be attributed to the inclusion of magnetic



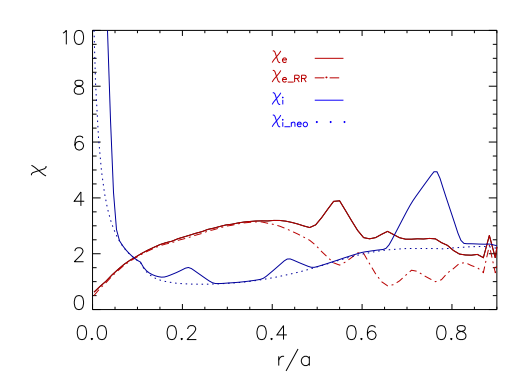
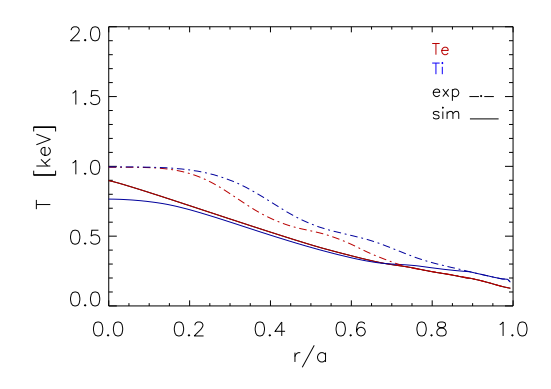


Figure 13. (Top panel) Experimental data (dash-dotted line) of ion and electron temperature profiles compared with simulation profiles (continuous lines) for the MAST-U case 47003 in electromagnetic transport model. (Bottom panel) Associated total ion and electron diffusion coefficient  $\chi_i$  and  $\chi_e$  in blue and red continuous lines respectively. Rechester-Rosenbluth  $\chi_{RR}$  and neoclassical diffusion  $\chi_{i_{neo}}$  coefficients in red dashed and blue dotted lines respectively. Diffusion coefficients are expressed in  $[m^2/s]$ .

fluctuations in  $TGLF(SAT1)EM^+$ .

 $RR_{c-less}+TGLF(SAT1)EM$  transport simulations for MAST-U #46978 give the profile predictions shown in Fig. 14. The top panel shows that both electron/ion profiles, and especially  $T_i$ , are underpredicted. Neoclassical transport, shown in the bottom panel, dominates the ion heat channel across most of the radial profile, and is similar to that in MAST-U #47003. Electron heat transport is lower than the ion heat transport, and is always dominated by stochasticity. Replacing TGLF(SAT1)EM by TGLF(SAT1)ES in the transport calculation results in



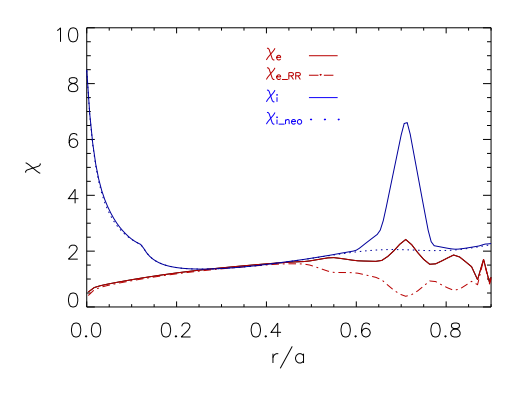
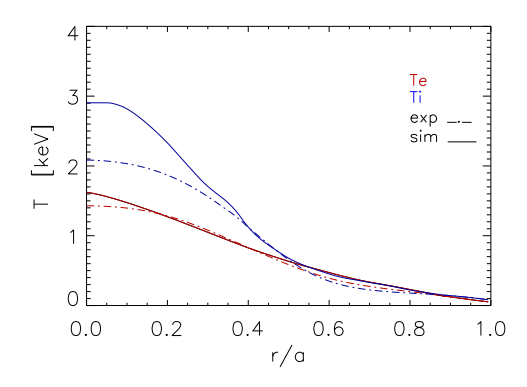


Figure 14. (Top panel) Experimental data (dash-dotted line) of ion and electron temperature profiles compared with simulation profiles (continuous lines) for the MAST-U case 46978 in electromagnetic transport model. (Bottom panel) Associated total ion and electron diffusion coefficient  $\chi_i$  and  $\chi_e$  in blue and red continuous lines respectively. Rechester-Rosenbluth  $\chi_{RR}$  and neoclassical diffusion  $\chi_{i_{neo}}$  coefficients in red dashed and blue dotted lines respectively. Diffusion coefficients are expressed in  $[m^2/s]$ .

extremely similar profile predictions, indicating that TGLF(SAT1)EM is not finding significant transport from electromagnetic modes in this discharge.

RR<sub>c-less</sub>+TGLF(SAT1)EM transport simulations for MAST #22664 are shown in Fig. 15. In this discharge the temperature profiles are over-predicted in both channels for r/a < 0.4. The RR modelled stochastic transport coefficients are notably larger than in both MAST-U H-mode discharges, and  $\chi_{RR}^{\text{c-less}}$  peaks at a value of  $5m^2/s$  around r = 0.3. As for #46978, replacing TGLF(SAT1)EM by TGLF(SAT1)ES has minimal impact on the transport steady state profiles, so the significant enhancement of  $\chi_e$  over  $\chi_{RR}$  at r/a > 0.4 predicted by TGLF can be attributed to electrostatic instabilities; ETG would be a likely candidate. Neoclassical ion heat transport still dominates the ion heat transport channel, but  $\chi_{i,neo}$  is rather lower than

<sup>&</sup>lt;sup>+</sup> The nature of the electromagnetic modes predicted by TGLF EM in this region will be investigated in future work, and may be due to the onset of hybrid-KBMs [69].



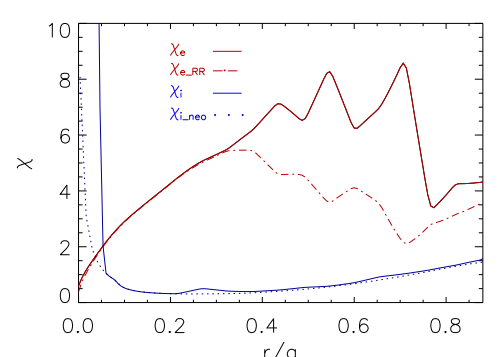


Figure 15. (Top panel) Experimental data (dash-dotted line) of ion and electron temperature profiles compared with simulation profiles (continuous lines) for the MAST-U case 22664 in electromagnetic transport model. (Bottom panel) Associated total ion and electron diffusion coefficient  $\chi_i$  and  $\chi_e$  in blue and red continuous lines respectively. Rechester-Rosenbluth  $\chi_{RR}$  and neoclassical diffusion  $\chi_{i_{neo}}$  coefficients in red dashed and blue dotted lines respectively. Diffusion coefficients are expressed in  $[m^2/s]$ .

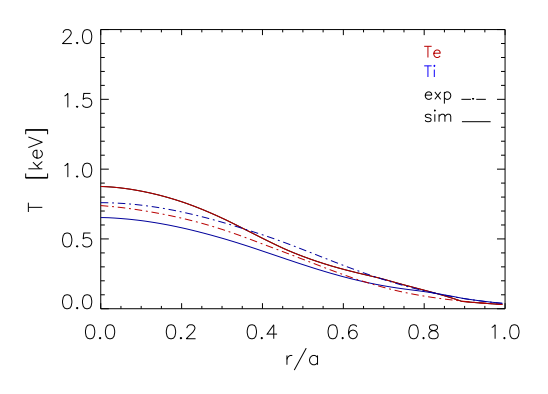
in the MAST-U discharges.

For the more ambiguous collisional discharge, #22769, with  $\lambda_{mfp} \approx l_{||c}$ , we adopt the following RR-hybrid model that should be more appropriate for describing the stochastic transport at transitional collisionality:

$$\chi_{e_{Hy}} = \left(\frac{1}{\chi_{e_{RR_{c-less}}}} + \frac{1}{\chi_{e_{RR_{coll}}}}\right)^{-1} \tag{28}$$

This model combines the RR-collisionless  $RR_{\rm c-less}$  and RR-collisional  $RR_{\rm coll}$  models, and accounts for collisionality increasing towards the edge because of the reduction in  $\lambda_{mfp}$ . Towards the edge we may expect to find  $\lambda_{mfp} < l_{||c}$ , which will reduce transport coefficients by a factor  $\lambda_{mfp}/l_{||c}$  with respect to the  $RR_{\rm c-less}$  model. Transport calculations using RR-

hybrid + TGLF(SAT1)EM for MAST #22769 are shown in Fig. 16. We note that transport calculations using this model for the other discharges find no substantial differences to the RR-collisionless results presented in Fig. 13, Fig. 14, and Fig. 15. This is because for these discharges  $\lambda_{mfp} > l_{||c}$  at least for  $r/a \lesssim 0.9$  after which we impose boundary conditions.



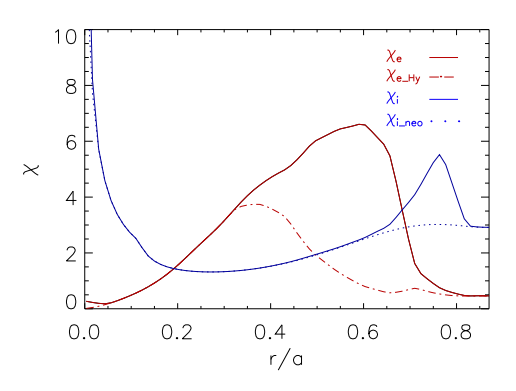


Figure 16. (Top panel) Experimental data (dash-dotted line) of ion and electron temperature profiles compared with simulation profiles (continuous lines) for the MAST case 22769 in electromagnetic transport model. (Bottom panel) Associated total ion and electron diffusion coefficient  $\chi_i$  and  $\chi_e$  in blue and red continuous lines respectively. Rechester-Rosenbluth  $\chi_{RR}$  and neoclassical diffusion  $\chi_{i_{neo}}$  coefficients in red dashed and blue dotted lines respectively. Diffusion coefficients are expressed in  $[m^2/s]$ .

An extension of this hybrid model will be developed in a future work. It is also interesting to note that  $\chi_e$  and  $\chi_{e_{RR}}$  are larger in the two MAST L-modes than in the MAST-U H-modes that we have examined. This is probably due to the different gradients involved and, as mentioned, to the fact that magnetic field is larger in the two MAST-U cases. Transport calculations using  $RR_{c-less}$  +

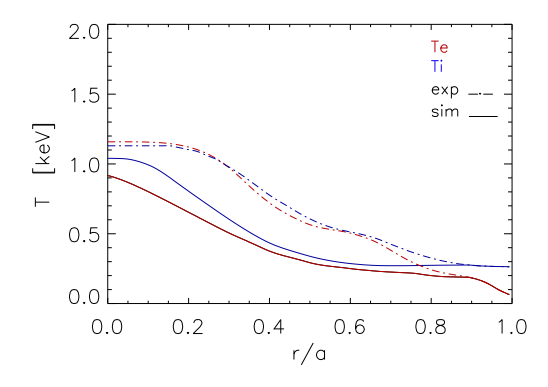
TGLF(SAT2)EM give significantly stronger transport, and flatter profiles: e.g. see transport calculation results for MAST-U #47003 in Fig. 17. Comparison of these profiles with SAT1 results in Fig. 12 shows that SAT2 gives higher electron (ion) heat diffusivities for r/a > 0.5 (r/a > 0.7). In particular, we observe that SAT2 predicted transport becomes extremely strong in correspondence of flat ion/electron temperature profiles when stochastic diffusivity assumes slow values. This is confirmed by removing flat ion profile and assuming an ion temperature profile with a gradient different from zero in the region r/a > 0.7. In this case, it is observed that ion heat diffusivity decreases at values lower than  $10m^2/s$ . This represents a clear indication of which points need to be investigated to improve the TGLF(SAT2) model.

Concerning results related to the RLW model, Fig. 18 shows example transport calculation results using RLW+TGLF(SAT1)EM for MAST-U #47003.

Comparing with the experimentally measured profiles, the modelled temperature profiles are much flatter at mid-radius and steeper in the core. The stochastic transport model,  $\chi_{e_{RLW}}$ , dominates the transport, though its profile is starkly different to that from the other RR stochastic models we have considered: in particular there is an enormous rise in  $\chi_{e_{RLW}}$  in the edge plasma, which is absent in  $\chi_{e_{RR}}$ . This edge enhancement appears in  $\chi_{e_{RLW}}$ principally due to the strong edge density gradient in the MAST-U plasma. Reducing the amplitude of the density gradient term in Eq. 19 would reduce the edge transport. Strong edge density gradients are typical in STs, resulting in RLW model predictions of very large transport when above the critical temperature gradient. The reason for including a density gradient term in a model of stochastic transport in tokamaks is not completely clear, though we note that in [44] the authors replaced  $L_T$  with  $L = (L_T^{-1} + Ln^{-1})^{-1}$  in a collisional reduced model of stochastic transport and found better agreement with the experimental estimate of the electron heat diffusivity from an NSTX H-mode plasma. However, there is no physical explanation for this empirical dependence and further study is needed.

It is also interesting to note from Fig. 19 that in MAST #22664 the temperature gradient exceeds the RLW critical gradient for the onset of stochastic transport of Eq. 19 across the whole radial cross-section, and that this has been observed in all the MAST shots we have studied.

As previously mentioned, the RLW model is only sensitive to collisionality, current density and other parameters, via the critical temperature gradient that sets the threshold. Thus the RLW model confinement scalings are insensitive to these quantities for plasmas in MAST, where  $|\nabla T_e| > |\nabla T_e|_c$  across the whole



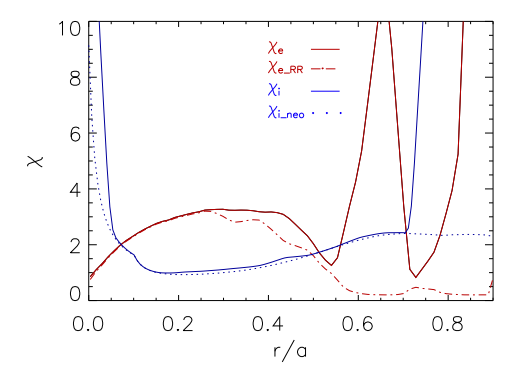
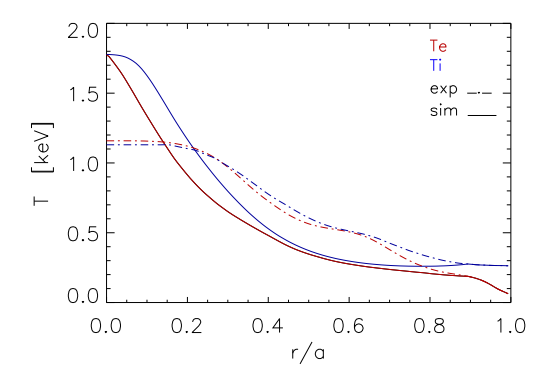


Figure 17. (Top panel) Experimental data (dash-dotted line) of ion and electron temperature profiles compared with simulation profiles (continuous lines) for the MAST-U case 47003 in electromagnetic transport model. (Bottom panel) Associated total ion and electron diffusion coefficient  $\chi_i$  and  $\chi_e$  in blue and red continuous lines respectively. Rechester-Rosenbluth  $\chi_{RR}$  and neoclassical diffusion  $\chi_{i_{neo}}$  coefficients in red dashed and blue dotted lines respectively. Diffusion coefficients are expressed in  $[m^2/s]$ . The used model has been the  $RR_{c-less}+TGLF(SAT2)$ .

plasma. This the RLW model cannot explain the strong favourable energy confinement scaling with collisionality that has been reported by ST experiments [5, 6, 70].

### 6.1. Summary of Model Validation

In order to summarize all the obtained results finalized to have an overview about the general behavior of the different models, we apply a systematic analysis to all the performed simulations. Thus, we present a systematic comparison of measured profiles from MAST and MAST-U against transport calculation predictions. This comparison is quantified for each



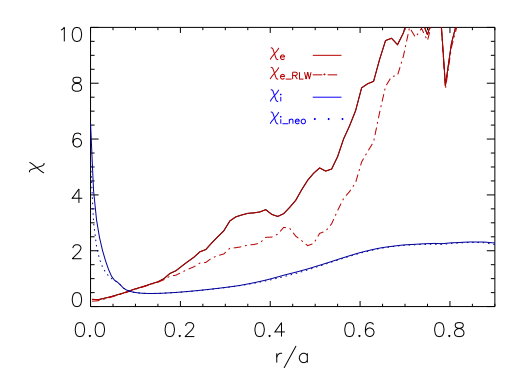


Figure 18. (Top panel) Experimental data (dash-dotted line) of ion and electron temperature profiles compared with simulation profiles (continuous lines) for the MAST-U case 47003 in electromagnetic transport model. (Bottom panel) Associated total ion and electron diffusion coefficient  $\chi_i$  and  $\chi_e$  in blue and red continuous lines respectively.  $\chi_{RLW}$  and neoclassical diffusion  $\chi_{i_{neo}}$  coefficients in red dashed and blue dotted lines respectively. Diffusion coefficients are expressed in  $[m^2/s]$ . The used model has been the RLW + TGLF(SAT1).

model prediction by computing the total squared fractional error,  $\chi^2$  to measure the quality of agreement with the measured profile.

We briefly summarise the principal characteristics of the method presenting the quantities used for the analysis. If there are  $x_D$  experimental data points  $D_{Exp,j}$  to compare with theoretical predictions, to quantify the discrepancy with data  $D_{Mod,j}$  of model, we may compute the  $\chi^2$  quantity given by:

$$\chi^2 = \sum_{j=1}^{x_D} \frac{\left(D_{Exp,j} - D_{Mod,j}\right)^2}{D_{Exp,j}^2} \tag{29}$$

The number obtained with this procedure must be compared with the number of degrees of freedom fd

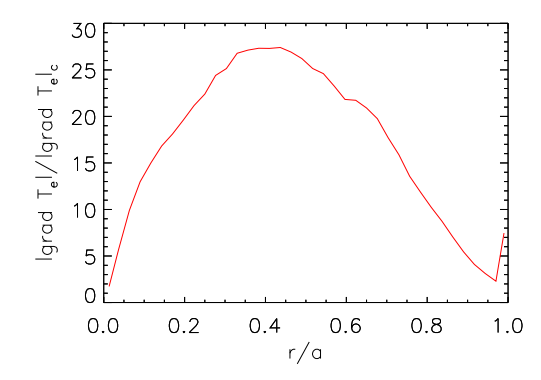


Figure 19. Ratio between temperature gradient and temperature gradient threshold for the case 22664.

that is defined as the number of data points  $x_D$  minus the number of free parameters fp in the model. The total squared fractional error per degree of freedom is given by the reduced  $\chi^2$ :

$$\bar{\chi}^2 = \frac{\chi^2}{fd} = \frac{\chi^2}{x_D - fp}$$
 (30)

Reduced  $\bar{\chi}^2$  results are shown in Fig. 20 and in Fig. 21 for the  $RR_{c-less}+TGLF(SAT1)$  and +TGLF(SAT2) respectively and in Fig. 22 for the RLW + TGLF(SAT1) model.

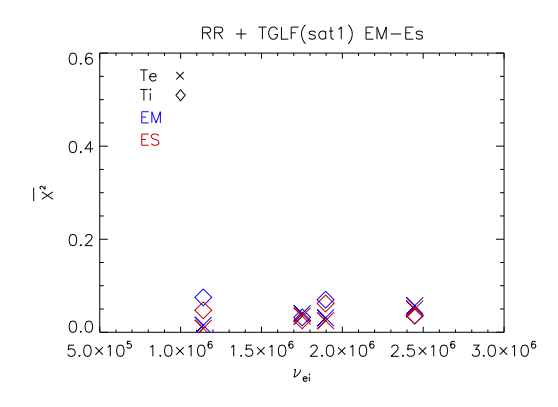


Figure 20. Reduced  $\bar{\chi}^2$  as a function of  $\nu_{ei}$  in  $[s^{-1}]$  for predictions obtained with the RR<sub>c-less</sub>+TGLF(SAT1) model for electrostatic (red) and electromagnetic (blue) regimes.

In this way, we are able to verify if simulation results are sufficiently close to experiments to decide the reliability of models for future predictions. The best values of  $\bar{\chi}^2$  have been obtained for the RR<sub>c-less</sub>+TGLF(SAT1) model. By observing Fig. 21

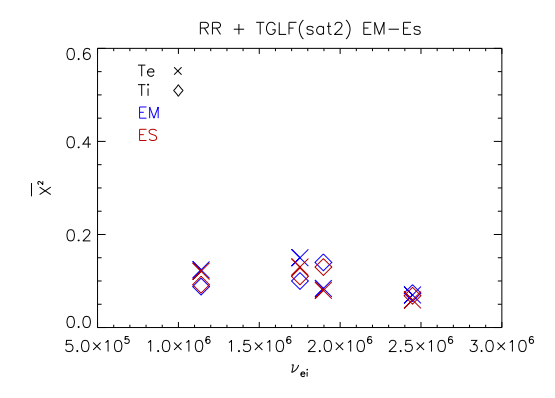


Figure 21. Reduced  $\bar{\chi}^2$  as a function of  $\nu_{ei}$  in  $[s^{-1}]$  for predictions obtained with the RR<sub>c-less</sub>+TGLF(SAT2) model for electrostatic (red) and electromagnetic (blue) regimes.

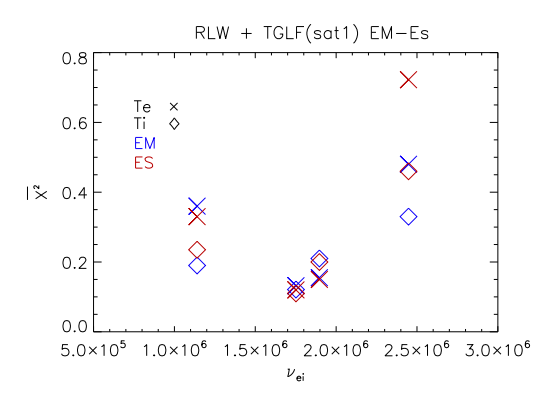


Figure 22. Reduced  $\bar{\chi}^2$  as a function of  $\nu_{ei}$  in  $[s^{-1}]$  for predictions obtained with the RLW+TGLF(SAT1) model for electrostatic (red) and electromagnetic (blue) regimes.

we can conclude that our simulations with reduced models and TGLF are in agreement with experimental data within the significant level of  $\approx 10\%$ . For  $\mathrm{RR_{c-less}}+$  TGLF(SAT2) simulations the value is  $\bar{\chi}^2_{max}\approx 0.15$ . Simulations related to RLW model show too large  $\bar{\chi}^2_{max}$  values and we can conclude that this latter model doesn't work very well for the studied cases. Within the level of  $\bar{\chi}^2_{max}\approx 0.10$  and  $\bar{\chi}^2_{max}\approx 0.15$  we can see what is the relative difference in stored energy  $W_{e,i}=\int 3/2K_BT_{e,i}ndV$ :

$$\Delta W_{e,i} = \frac{W_{e,i_{sims}} - W_{e,i_{exp}}}{W_{e,i_{exp}}} \tag{31}$$

between experiments and simulations for ions and electrons in the different studied cases.

These quantities are plotted in the histogram of Figs. 23, 24, 25 for RR+TGLF(SAT1),

RR+TGLF(SAT2) and RLW+TGLF(SAT1) respectively. Electrostatic and electromagnetic simulations are indicated in red and in blue colors respectively, while ion and electron stored energy quantities are indicated in lighter and darker tones. In agree-

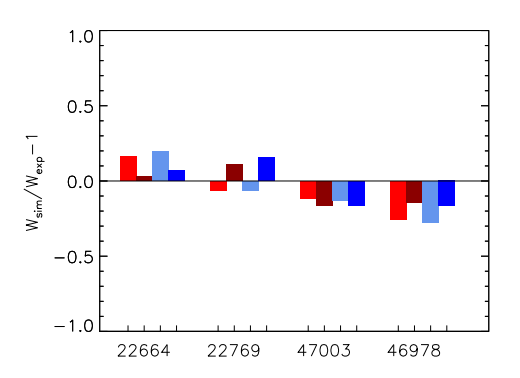


Figure 23. Histogram of stored energy difference  $\Delta W_{e,i}$  for the examined shots by adopting the RR+TGLF(SAT1) model. Electrostatic and electromagnetic setup are indicated by using red and blue color respectively. The lines corresponding to ion and electron are indicated by light and dark colors respectively. Thus from left to rigth we have the corresponding ion-, electron-electrostatic and ion- and electron-electromagnetic lines.

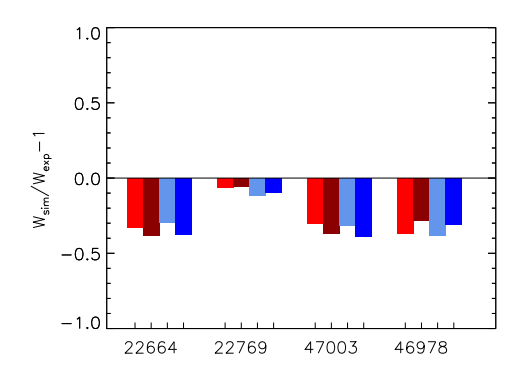


Figure 24. Histogram of stored energy difference  $\Delta W_{e,i}$  for the examined shots by adopting the RR+TGLF(SAT2) model. Electrostatic and electromagnetic setup are indicated by using red and blue color respectively. The lines corresponding to ion and electron are indicated by light and dark colors respectively. Thus, from left to right we have the corresponding ion-, electron-electrostatic and ion- and electron-electromagnetic lines.

ment with  $\chi^2$  analysis the best results have been obtained for RR+TGLF(SAT1) case at which we can as-

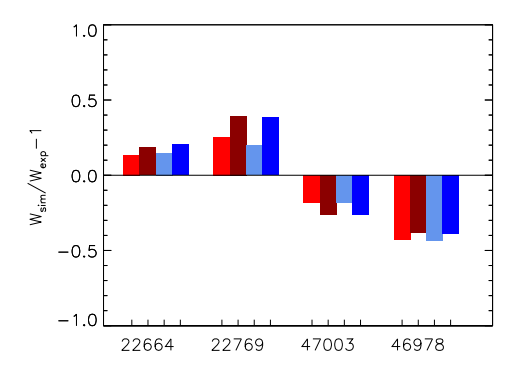


Figure 25. Histogram of stored energy difference  $\Delta W_{e,i}$  for the examined shots by adopting the RLW+TGLF(SAT1) model. electrostatic and electromagnetic setup are indicated by using red and blue color respectively. The lines corresponding to ion and electron are indicated by light and dark colors respectively. Thus from left to right we have the corresponding ion-, electron-electrostatic and ion- and electron-electromagnetic lines.

sociate a  $\Delta W_{imax} \approx \Delta W_{emax} \approx 20\%$ . Very good results have been obtained for the stored electron energy for the two L-mode cases. Moreover, we observe that the best results are related to the RR+ electrostatic TGLF version. The use of the electrostatic version gives slightly better results than electromagnetic version because probably part of EM effects are considered at the same time by reduced stochastic model and by TGLF. These point will be investigated in a future work. However, results obtained by coupling RR+TGLF(SAT1) appear quite promising. Concerning the use of SAT2 we have an energy disagreement  $\Delta W_{imax} \approx \Delta W_{emax} \approx 40\%$ . Good results have been obtained only for the MAST case 22769, but this is only achieved for the total stored energy because radial regions where the simulated pressure exceeds the experimental profile, compensate for regions in which simulation pressure under-predicts the experimental profile. By considering results obtained with the RR+TGLF(SAT1) model, in Fig. 26 we plot the ratio between the averaged quantities of  $X_{e_{RR}}$  and  $X_e$ as a function of  $\langle \lambda_{mfp} \rangle / \langle l_{||c} \rangle$ . The red line is referred to the ratio  $\langle X_{e_{RR}} \rangle / \langle X_e \rangle$ , whose quantities  $\langle X_{e_{RR}} \rangle$  and  $\langle X_e \rangle$  are respectively averaged in the central radial region r/a = [0.45, 0.75] as for  $\langle \lambda_{mfp} \rangle$  and  $\langle l_{\parallel c} \rangle$ . Green line has been obtained by considering average  $\langle X_{e_{RR}} \rangle$ and  $\langle X_e \rangle$  along the radial direction until to the boundary conditions at r/a = 0.9. In this way, it is possible to obtain a trend about the importance of the stochastic transport played in the different scenarios. It emerges that by moving from a more collisional regime in which

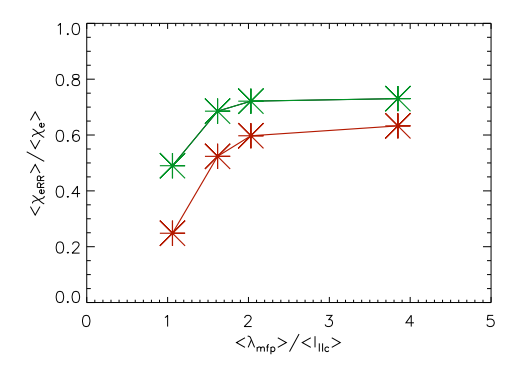


Figure 26. Ratio between averaged quantities of  $X_{e_{RR}}$  and  $X_e$  as a function of  $\langle \lambda_{mfp} \rangle / \langle l_{||c} \rangle$ . The red line is referred to the ratio of average  $\langle X_{e_{RR}} \rangle$  and  $\langle X_e \rangle$  respectively, in the central radial region r/a = [0.45, 0.75], while green line is referred to the ratio of average  $\langle X_{e_{RR}} \rangle$  and  $\langle X_e \rangle$  along the radial direction until to the boundary conditions at r/a = 0.9.

 $\langle \lambda_{mfp} \rangle \approx \langle l_{||c} \rangle$  towards to a collisionless regime in which  $\langle \lambda_{mfp} \rangle \gg \langle l_{||c} \rangle$  the stochastic transport importance increases. This suggest the possibility to control the role of stochasticity in the different scenarios in tokamaks and in particular in STs via the parameters involved in two important scales represented by  $\lambda_{mfp}$  and  $l_{||c}$ . Thus, this work can be useful in the predictions of ITER scenarios and in the conception of the STEP design.

An exhaustive investigation on this latter subject will be developed in a devoted paper. However, in the light of this work, could be interesting to make few estimations and briefly considerations about the transport characteristics in STEP. Regarding the applicability of stochastic model for STEP prediction we can observe that the mean free path estimate for STEP is  $\lambda_{mfp} \approx 800 \text{m}$ . This value can be compared to  $l_{||c} \approx 12 \text{ m}$  for STEP suggesting the use of RR-collisionless model as the best model for reliable predictions.

Preliminary results have been obtained by using  $RR_{c-less}$  and Bohm, gBohm models with coefficients values for ion and electrons adopted in JET studies and described in Ref. [72]. Bohm contribution has been regulated by:

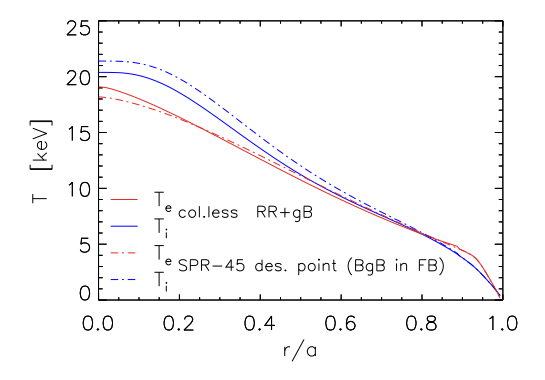
$$\chi_{gB_e} \propto \frac{a_0}{B_{ax}} \frac{|\partial P_e/\partial \rho|}{n_e} q^2 \quad X_{B_i} = 2\chi_{B_e}$$
(32)

and gyroBohm contribution has been calculated by:

$$\chi_{gB_e} \propto \frac{\sqrt{Te}}{B_{ax}^2} \left| \frac{\partial T_e}{\partial \rho} \right| \quad X_{gB_i} = 0.5 \chi_{gB_e}$$
(33)

with  $a_0 = (R_{out} - R_{in})/2$  and  $\rho = \sqrt{\Phi/(\pi B_0)}$ . Obtained results are very encouraging, showing

simulation equilibrium profiles very close to the desired ones as indicated in the top panel of Fig. 27. Bottom panel indicates that the dominant transport mechanism is stochastic with a small contribution due to the gBohm effect. The impact of the stochastic transport is in agreement with the trend obtained in Fig. 26, according to which moving towards a scenario with  $\langle \lambda_{mfp} \rangle \gg \langle l_{||c} \rangle$ , the importance of stochasticity increases.



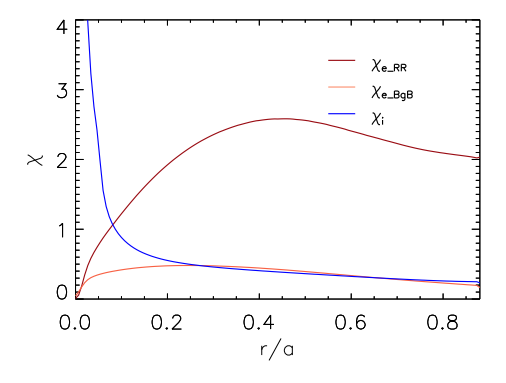


Figure 27. (Top panel) Comparison between SPR-45 design point for STEP and profiles obtained by using  $RR_{c-less} + Bohm$  gyroBohm model. (Bottom panel) Transport diffusion coefficient profiles in  $[m^2/s]$  units for RR and gyroBohm parts respectively.

## 7. Conclusion

Electromagnetic turbulence is likely to be very important for future plasma regimes, including at high  $\beta$  and in STs, and is therefore of considerable interest to the fusion community. Physics-based reduced models of core transport are essential to improve our confidence in integrated scenario modelling for future tokamak plasmas, and these models are less

well developed and validated for plasmas where the core turbulence is electromagnetic in character. Microtearing modes, for example, are expected to generate stochastic fields that cause anomalous electron heat transport in such plasmas.

In this work we have implemented, in the JIN-TRAC integrated modelling suite, three reduced models of anomalous electron heat transport from stochastic magnetic fields: RR-collisionless; RR-collisional; and the RLW model. Stochastic field dynamics provide a parallel mechanism for electron heat transport, which complements other transport processes from electrostatic/electromagnetic turbulence that can be described by the TGLF model, and neoclassical transport that can be calculated using NCLASS. Four steady discharges suitable for transport analysis have been identified from MAST and MAST-U that span a range in parameters including collisionality. have tested combinations of the stochastic models with TGLF and NCLASS by performing JINTRAC transport simulations for the MAST and MAST-U plasmas. Inspection of the parameters of the MAST and MAST-U plasmas suggests that the RR-collisionless model is the most suitable collisional regime to describe these experiments\*. We have also proposed a hybrid variant of the RR model to span collisional regimes. Best transport predictions for the four discharges have been obtained using the RR-collisionless+TGLF(SAT1)ES model. In the framework of the transport, results show a trend for which the importance of the stochasticity with respect to the other electrostatic/electromagnetic instabilities increases by increasing the  $\langle \lambda_{mfp} \rangle / \langle l_{||c} \rangle$  ratio. This trend could be very useful in the control of the role of stochasticity in tokamak scenarios. Replacing SAT1 with the SAT2 saturation rule in TGLF renders the predictions less accurate. RLW+TGLF does much less well than the RR+TGLF models, suggesting that the Rechester-Rosenbluth approach more faithfully captures the stochastic transport.

More effort will be required to further improve and more extensively validate reduced transport models for electromagnetic turbulence, either within quasilinear models like TGLF, or by complementing its approach as proposed here for stochastic fields using RR-based models.

## Acknowledgments

#### References

- L. Spitzer jr: A proposed stellarator. AEC Research and Development Report NYO-993, United States Atomic Energy Commission, Washington D.C. (1951) 156 5. A.I. Morozov, L.S. Solovev: Motion of charged particles in electro-magnetic fields. In: Reviews of Plasma Physics,
- \* This is also the most suitable collisional regime for STEP.

- vol 2 ed by M.A. Leontovich (Consultants Bureau, New York 1966) pp 201-297 157
- [2] Sykes A. et al. 1994 Nucl. Fusion 32, 769
- [3] Gerhardt S.P. et al. 2011 Nucl. Fusion 51 073031
- [4] Sabbagh S.A. et al. 2013 Nucl. Fusion 53 104007
- [5] Valovic M. et al. 2011 Nucl. Fusion 51 073045
- [6] Kaye S.M. et al. 2021 Plasma Phys. Control. Fusion 63 123001
- [7] Gryznevich M. et al 1998 Phys. Rev. Lett. 80 3972
- [8] Kaye S. M. et al. 1999 Fusion Technol. 36 16
- [9] Ono M. et al 2001 Nucl. Fusion 41 1435
- [10] Gartska G.D. et al. 2003 Phys. Plasmas 10 1805
- [11] Darke A.C. et al. 1995 Fusion Technol. 1 799
- [12] V.K. Gusev et al 2009 Nucl. Fusion 49 104021
- [13] V B Minaev et al 2018 J. Phys.: Conf. Ser. 1094 012001
- [14] MAST Upgrade Research Plan, November 2019, Culham Centre for Fusion Energy. Retrieved 2020-10-26.
- [15] M Gryaznevich et al 2017 Fusion Engineering and Design  $123\ 177$
- [16] J W Berkery et al, 2024 Nucl. Fusion 64 112004
- [17] E. Tholerus et al 2024 Nucl. Fusion 64 106030
- [18] Roach C. M. et al 2009 Plasma Phys. Control. Fusion 51 124020
- [19] Palermo F. et al. 2015 Phys. Plasmas 22 042304
- [20] Palermo F., Garbet X. and Ghizzo A. 2015 Europ. Phys. Journal D 69, 8
- [21] Ghizzo A. and Palermo F., 2015 Phys. Plasmas 22 082303
- [22] Ghizzo A. and Palermo F., 2015 Phys. Plasmas
- [23] Wang W X et al 2015 Phys. Plasmas 22 102509
- [24] Guttenfelder W et al 2019 Nucl. Fusion 59 056027
- [25] Ren Y. et al 2017 Nucl. Fusion 57 072002
- [26] Giacomin M, et al 2023 Plasma Phys. Control. Fusion 65 095019
- [27] Guttenfelder W et al 2011 Phys. Rev. Lett. 106 155004
- [28] Giacomin M et al 2024 Plasma Phys. Control. Fusion 66 055010
- [29] Applegate H. et al 2007 Plasma Phys. Control. Fusion 49 1113
- [30] Doerk H. et al 2011 Phys. Rev. Lett. 106 155003
- [31] Dickinson D. et al 2012 Phys. Rev. Lett. 108 155003
- [32] Connor J.W. et al 2006 Proc. 21st IAEA Conf. on Fusion Energy (Chengdu, China, 2006) TH2/P2-2
- [33] W. Guttenfelder, J. Candy, S. M. Kaye, W. M. Nevins, E. Wang, J. Zhang, R. E. Bell, N. A. Crocker, G. W. Hammett, B. P. LeBlanc, D. R. Mikkelsen, Y. Ren, and H. Yuh, Phys. Plasmas 19, 056119 (2012).
- $[34]\;$  Hardman M R et al 2023 Plasma Phys. Control. Fusion 65 045011
- [35] B.S. Patel et al. 2024 to be submitted to PPCF
- [36] Staebler G M, Kinsey J E and Waltz R E 2007 Phys. Plasmas 14 055909
- [37] Staebler G M et al 2008 Testing the trapped gyro-Landau fluid transport model with data from tokamaks and spherical tori Proc. 22nd IAEA Fusion Conf. (Geneva, Switzerland) p TH/P8-42
- [38] Avdeeva et al. Nuclear Fusion 2023
- [39] Rechester, Rosenbluth 1979 Phys. Rev. Letter 40, 1
- [40] Rechester, Rosenbluth, White 1979 Phys. Rev. Letter 42, 19
- [41] Rafiq T. et al. 2016 Phys. Plasmas 23, 062507
- [42] Rafiq T. et al. 2021 Phys. Plasmas 28, 022504
- [43] P.H. Rebut, P.P. Lallia, M.L. Watkins, IAEA-CN-50/D-IV-1 (1984)
- [44] K. L. Wong Phys. Rew. Letter 99, 135003, 2010
- $[45]\;$  Kaye S M et al 2014 Phys. Plasmas 21 082510
- [46] M. Romanelli, Plasma and Fusion Research 9, 3403023 (2014)
- [47] Pereverzev G.V. et al. 1991 ASTRA an automated system for transport analysis, IPP Report 5/42, Max-Planck-Institut fuer Plasmaphysik

- [48] M. N. Rosenbluth, R.Z. Sagdeev (eds.), Handbook of Plasma Physics (North-Holland, Amsterdam, 1984)
- [49] A. N. Kolmogorov 1959 Dokl. Akad. Nauk. USSR 98, 527
- [50] J. D. Farmer 1982 Information Dimension and the Probabilistic Structure of Chaos, Z. Naturforsh. 37a, 1304
- [51] J. A. Krommes, et al. J. Plasma Physics 1983, 30, 56
- [52] S. Wiesen et al., JET ITC-Report (2008).
- [53] R.E. Waltz et al., Phys. Plasmas 4, 2482 (1997).
- [54] H. Nordman et al., Nucl. Fusion 30, 983 (1990).
- [55] J. F. Drake and Y. C. Lee, Phys. Fluids 20, 1341 (1977).
- [56] Doerk H. et al 2012 Phys. Plasmas 19 055907
- [57] R.W. Harvey, M. G. McCoy, J.Y. Hsu, and A. A. Mirin, 1981 Phys. Rev. Lett. 47 102.
- [58] W.M. Nevins et al. 2011 Phys. Rev. Lett. 106 065003
- [59] H Doerk et al 2016 Plasma Phys. Control. Fusion 58 115005
- [60] Staebler G. M. et al. 2007 Phys. Plasmas 14 055909
- [61] G.M. Staebler, J. Candy, N.T. Howard and C. Holland, 2016, Physics of Plasmas 23, 062518
- [62] G.M. Staebler, E. A. Belli, J. Candy, J.E. Kinsey, H. Dudding and B. Patel, Nuclear Fusion 61, 116007, (2021)
- [63] H.G. Dudding, F.J. Casson, D. Dickinson, B.S. Patel, C.M. Roach, E.A. Belli and G.M. Staebler, Nuclear Fusion 62, 0960005, (2022)
- [64] Zaslavsky VG. M. and Chirikov B. V. 1972 Sov. Phys. Usp. 14, 549
- [65] Baiocchi B. et al. 2015 Plasma Phys. Control. Fusion 57 035003
- [66] McClenaghan J. et al. 2017 Nucl. Fusion 57 116019
- [67] C. Pan et al. 2017 Nucl. Fusion 57 036018
- [68] Staebler G M et al 2008 Testing the trapped gyro-Landau fluid transport model with data from tokamaks and spherical tori Proc. 22nd IAEA Fusion Conf. (Geneva, Switzerland) p TH/P8-42
- [69] D. Kennedy et al., 2023, Nucl. Fusion 63, 126061
- [70] S.M. Kaye et al., 2013, Nucl. Fusion 53 063005
- [71] X. Garbet et al. 2010 Nucl. Fusion 50 043002
- [72] M. Erba et al., Pl. Phys. Control. Fusion 39, 261 (1997).